Ocean Dynamics (2007) 57: 205–221
DOI 10.1007/s10236-007-0103-8

Lie-Yauw Oey · Tal Ezer · Chuanmin Hu ·
Frank E. Muller-Karger

Baroclinic tidal flows and inundation processes in Cook Inlet, Alaska: numerical modeling and satellite observations

Received: 7 September 2006 / Accepted: 26 January 2007 / Published online: 3 March 2007

Abstract A wetting and drying (WAD) algorithm is implemented in a baroclinic three-dimensional ocean circulation model of Cook Inlet, Alaska, where large tidal ranges (≈10 m) regularly expose extensive mudflats. The model includes tides and wind- and buoyancy-induced flows. In the upper Inlet, the model successfully simulates large amplification of tides and propagation of fast (3~4 m s^{-1}) tidal bores over shallow mudflats. The simulated return flows during ebb expose large areas (~100 km^2) of the mudflats. Medium-resolution (250- and 500-m) images obtained from the moderate resolution imaging spectroradiometer (MODIS) instruments aboard the Terra and Aqua satellites were used to verify the model results by identifying the location, extent, and temporal changes of the exposed mudflat regions. The results demonstrate the value of operational, medium-resolution remote sensing data in evaluating the WAD model. Sensitivity tests show that WAD produces approximately 20% larger tidal amplitude and 10% slower phase than the corresponding experiment without WAD. In the deep channel of the central Inlet, the confluence of saline water of the lower Inlet with brackish water from rivers and melting ice from land around the upper Inlet produces a salinity front. At the simulated front, strong vertical circulation cells and surface convergence and currents develop, especially during the flood. The characteristics resemble those of "rip tides" often observed in this region.

Keywords Numerical model · Tides · Inundation · Satellite data · MODIS · Alaska

Responsible editor: Jörg-Olaf Wolff

L.-Y. Oey
Program in Atmospheric and Oceanic Sciences,
Princeton University,
P.O. Box CN710, Sayre Hall,
Princeton, NJ 08544-0710, USA

T. Ezer (✉)
Department of Ocean Earth and Atmospheric Sciences,
Old Dominion University,
Norfolk, VA 23529, USA
e-mail: ezer@splash.princeton.edu
Tel.: +1-609-2581318
Fax: +1-609-2582850

C. Hu · F. E. Muller-Karger
Institute for Marine Remote Sensing,
College of Marine Science, University of South Florida,
St. Petersburg, FL 33701, USA

1 Introduction

Wetting and drying (WAD) is a common and important phenomenon of the coastal ocean and estuaries, especially over low-lying coastal zones. In bays and inlets with large amplitude tides, such as in the Bay of Fundy (Gulf of Maine) and the Cook Inlet (Alaska), WAD is an essential part of the local environment and ecosystem. In extreme cases, the effects of WAD are dramatic and tragic, as demonstrated recently during the Indian Ocean tsunami (December 2004) and the flooding of New Orleans by hurricane Katrina (August 2005). WAD modeling is clearly of practical importance, but until recently, WAD schemes have been implemented mostly in hydraulic and in coastal/estuarine models (Stelling et al. 1986; Balzano 1998; Lynch and Gray 1980; Flather and Hubbert 1990; Casulli and Cheng 1992; Lin and Falconer 1997; Ji et al. 2001; Xie et al. 2004; Chen et al. 2006). However, as various regional and large-scale ocean general circulation models (OGCMs) and forecast systems evolve (Chassignet et al. 2003; Drillet et al. 2005; Ezer and Mellor 2000; Fan et al. 2004; Ko et al. 2003; Marchesiello et al. 2003; Romanou et al. 2004; Sheng and Tang 2003; Smith et al. 2000; Oey et al. 2003, 2005), the distinction between the coast and open ocean becomes blurred, and there is a need to include dynamic (or movable) coastal boundaries to model inundation processes. The first such OGCM using the Princeton ocean model (POM; Blumberg and Mellor 1987; Mellor 2004) has recently been developed and described in Oey (2005, 2006). In these latter papers, idealized one-, two-, and three-dimensional cases such as the dam-break, "water fall," tsunami, tidal, and estuarine-circulation problems

were tested. The POM–WAD implementations rely on the vast experiences of coastal and estuarine modelers (cited above), but are unique in two important ways. Firstly, the WAD algorithm is implemented in a three-dimensional baroclinic ocean forecast system that is equipped with data assimilative tools, nesting capabilities, and large-scale and regional forcing (see http://www.aos.princeton.edu/WWWPUBLIC/PROFS/ and publications listed therein). Secondly, the WAD conditions across the cells' interfaces are fully dynamic using the full set of primitive equations. In this paper, we describe the model implementations and results for Cook Inlet, Alaska, where the tidal range reaches 10 m and active WAD physics exist. We will also evaluate the simulated WAD processes with repeated medium-resolution remote sensing imagery.

Cook Inlet, Alaska, is named after the English explorer James Cook (1728–1779) who, in 1778, sailed along the northwestern coast of North America and the Bering Strait (Beaglehole 1974). The Inlet extends approximately 250~300 km from the Gulf of Alaska in the south into the city of Anchorage in the northeast where it branches into two shallower extensions, the Knik Arm north of Anchorage and the Turnagain Arm southeast of Anchorage (Fig. 1). The water levels and currents in Cook Inlet are strongly

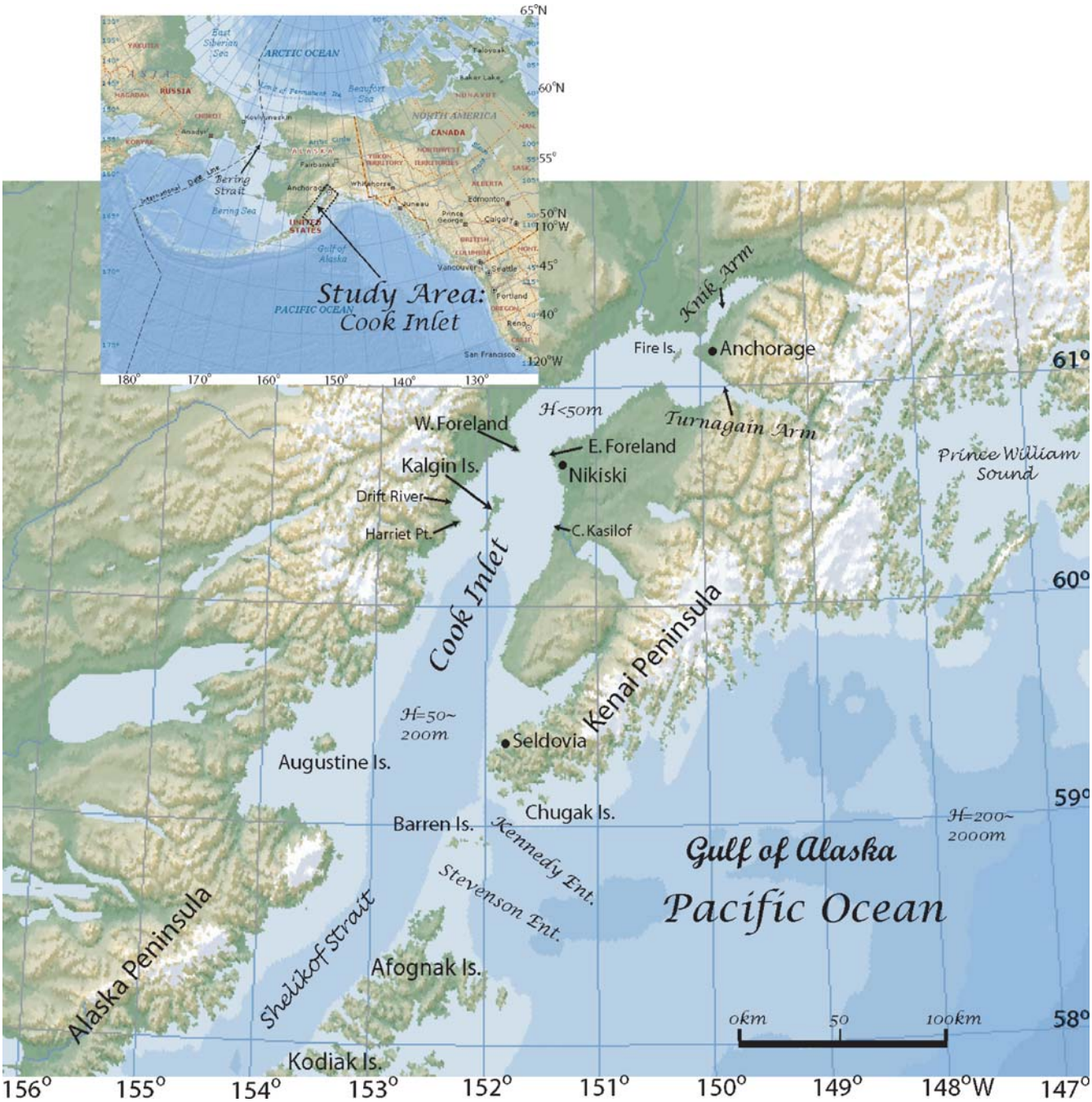

Fig. 1 Map of the Cook Inlet region in the northeastern Pacific (*small inset*) and the major (crude) topographic and geographic features

influenced by tides from the Gulf of Alaska. The 'tidal resonant' length scale can be estimated by $(gH_{ave})^{1/2}P/4\approx$ 250 km (Gill 1982), where g=9.8 m s^{-2} is the gravitational constant, $P\approx$12.42 h is the M_2 tide period, and $H_{ave}\approx$50 m is the Inlet's averaged water depth. This resonant scale is close to the Inlet's length; as a result, tides are significantly

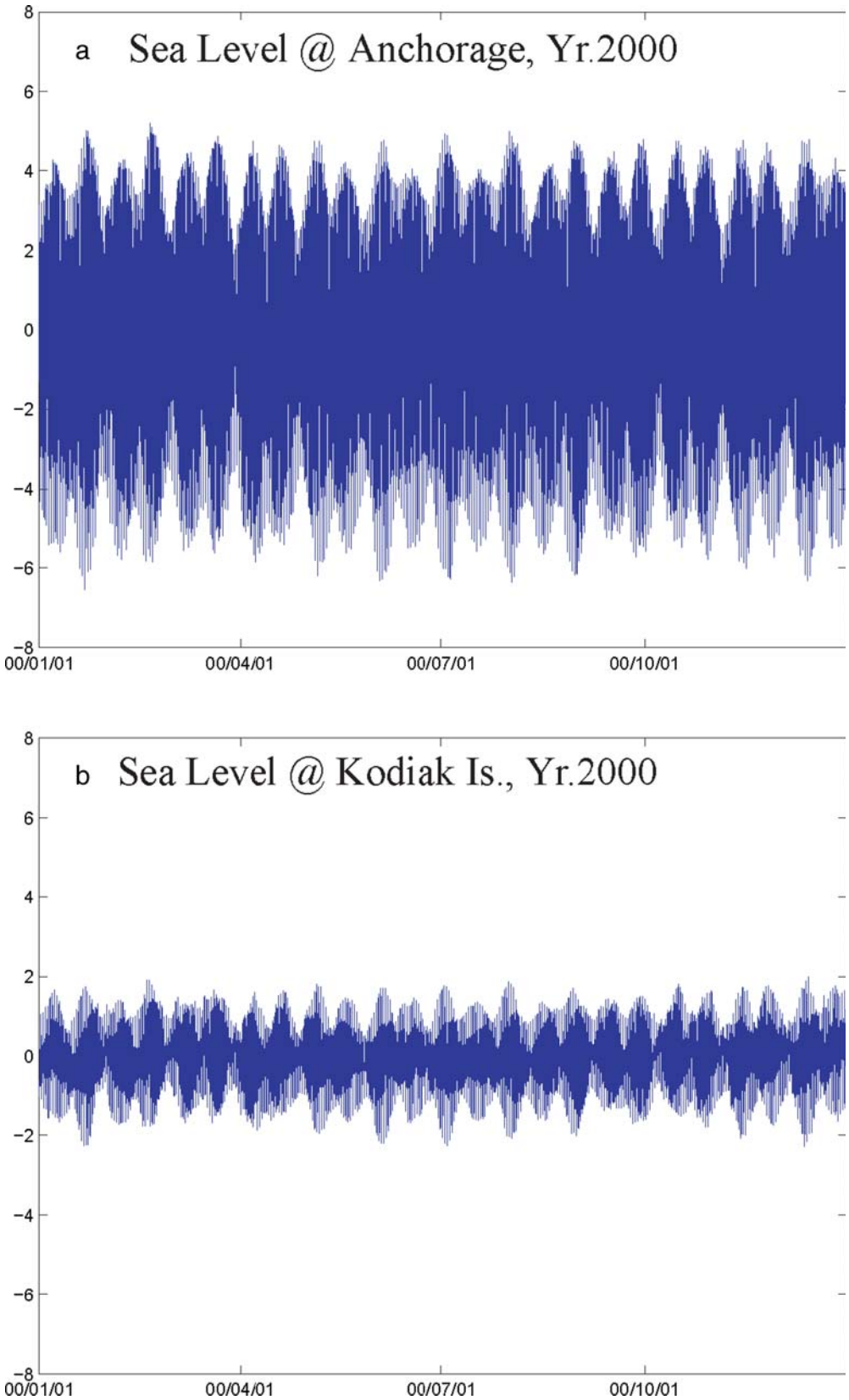

Fig. 2 Observed hourly sea level (in meters) at **a** Anchorage and **b** Kodiak Island during 2000

amplified from about ±1 m near the Gulf of Alaska, opening to about ±5 m in the northern Inlet (Fig. 2). The large tide produces strong currents and tidal bores with speeds ~4 m s^{-1} and peak heights ~3 m in the Turnagain Arm during a flood (http://www.tidal-bore.tripod.com/usa/turnagain.html), and exposes extensive mudflats throughout the upper Inlet in the subsequent ebb. WAD is, therefore, a common and important phenomenon in the Cook Inlet. The extensive mudflats are visible from specially processed satellite images that will be used to validate the model. In the central portion of Cook Inlet, strong oscillatory tidal currents in channels are often associated with the so-called rip tides (Haley et al. 2000; Okkonen and Howell 2003); using the model calculations, we will investigate possible mechanisms for this phenomenon.

In addition to tides and WAD, currents induced by buoyancy (from rivers) and winds also constitute important components of the circulation and mixing in the Cook Inlet. Figure 3 shows the monthly discharges from seven major rivers obtained from the US Geological Survey (USGS). However, tributary discharges are significant, and the combined high discharge during spring/summer snow melt amounts to over 5×10^3 m^3 s^{-1}, or approximately 2~3 times the combined peak discharge shown in Fig. 3. The river freshening, as well as the tidal and wind mixing, results in a partially mixed estuary. The surface salinity S in the lower Inlet near the Stevenson–Kennedy entrance is ≈30~32 psu, which is a little less than the salinity values found over the adjacent shelf/slope in the Gulf of Alaska (Xiong and Royer 1984). The Cook Inlet/Gulf of Alaska climate is extreme. Winter storms associated with the Aleutian Low propagate to the Gulf of Alaska from the northwestern Pacific (Wang et al. 2004). These storms and continental drainage winds bring high wind speeds (over 20 m s^{-1}) and frigidly low air temperatures. The mean winter wind is generally westward. In summer, the Aleutian Low is replaced by a high-pressure system (Wang et al. 2004), resulting in a generally eastward (and much weaker) wind (Royer 1975).

The paper is organized as follows. Section 2 describes the Cook Inlet model setup. In Section 3, we discuss tides, tidal bores, and WAD processes in the upper Inlet, and compare the modeled WAD regions with remote sensing data. Section 4 examines the role of buoyancy and tides in producing 'rip tides' in the central Inlet, and Section 5 concludes the paper.

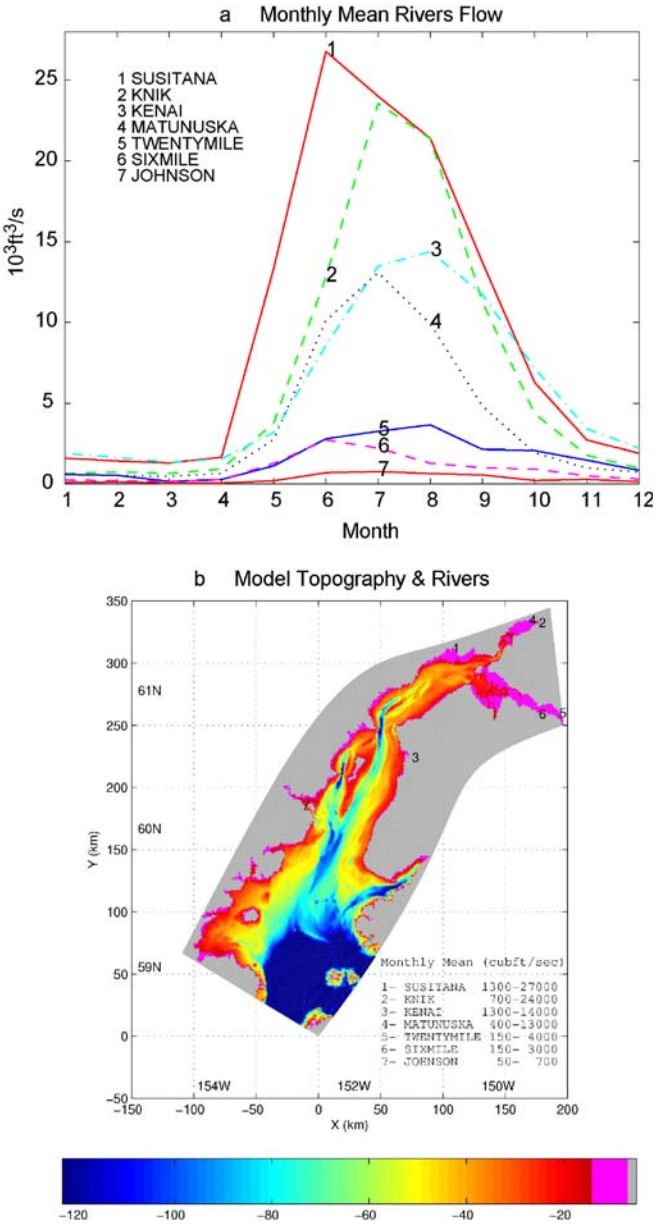

Fig. 3 **a** USGS monthly mean river discharges (plotted in the original unit in ft^3 s^{-1}; 1 m^3 s^{-1}≈27 ft^3 s^{-1}) from seven major rivers into the Cook Inlet. **b** Location of the seven rivers marked on the model topography (in meters below a land datum; see Oey 2006). The *gray* represents the absolute land region that is always dry; the *magenta* represents the WAD region that can be wet or dry

2 The Cook Inlet model setup

The model is based on POM: three-dimensional with curvilinear horizontal grid, terrain-following ("sigma") vertical grid and Mellor and Yamada's (1982) mixing. It incorporates a WAD algorithm that is described in great details in Oey (2005, 2006). At each time step, a cell's face is blocked if the local water depth is less than a prescribed value (=5 cm is used) by setting the corresponding fluxes=0. The requirement that cells must be slightly wet is consistent with Wang's (1996) numerical stability condition for shallow-water equations. The model solves the full set of governing equations over wet as well as dry cells and flows across cell faces satisfy the balance equations, which dictate if the cells become wet or dry at the next time step. Dry cells are, thus, temporarily dormant, to be activated depending on volume and momentum conservations in that cell as well as in the neighboring cells (heat and salt fluxes are also activated for general stratified flows).

WAD simulations require bottom topography from deep waters to absolute land regions where the orography is sufficiently high that grid cells are *always* dry. The

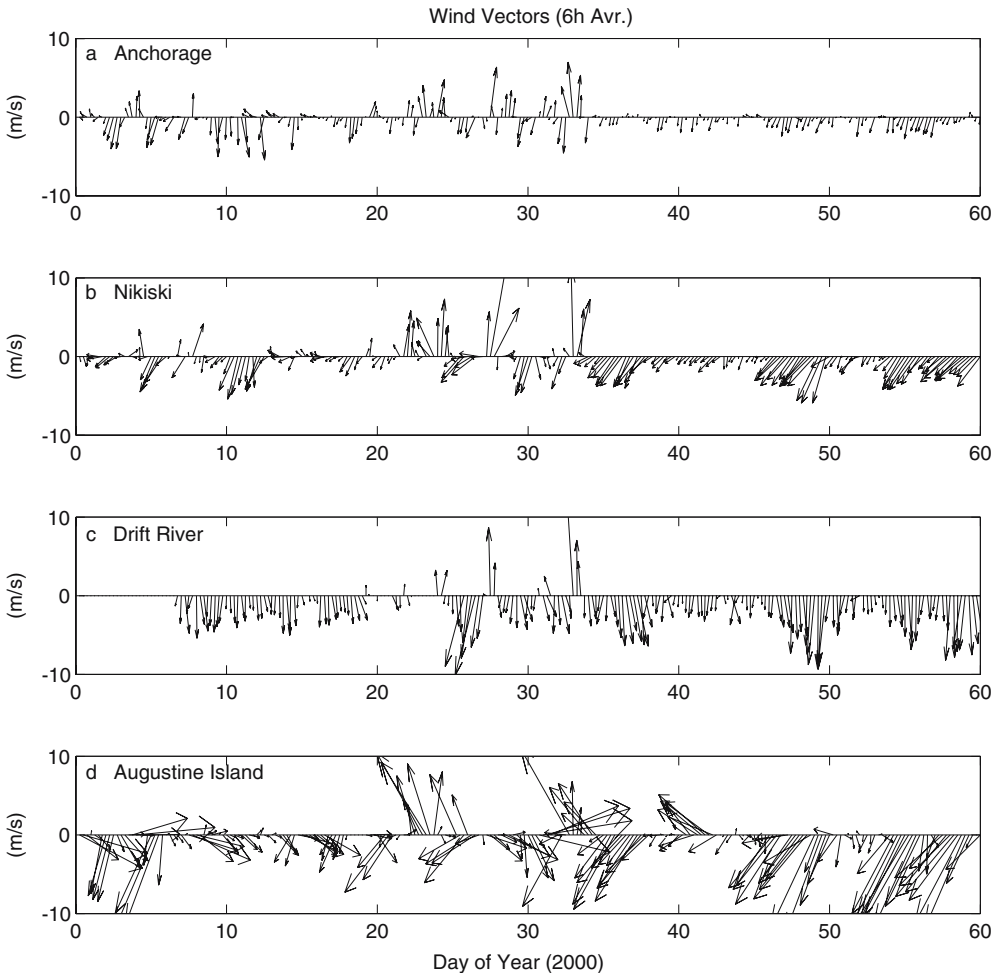

Fig. 4 The observed wind vector stick plot at four stations for the first 60 days of the year 2000; six hourly averages were calculated from the NOAA meteorological stations

transition (of the potential WAD region) is not well defined for Cook Inlet especially over the mudflats. On the other hand, the National Oceanic and Atmospheric Administration/National Ocean Service's (NOAA/NOS) nautical charts (sounding data) do delineate potential WAD regions for boaters. We, therefore, interpolated the topography data set without WAD regions (which was on a 1×1-km grid kindly provided by Dr. Proshuntinsky, Woods Hole Oceanographic Institution, WHOI) with NOAA's potential WAD regions so that the depth tapers to zero at the nearest absolute land points. The final depths for all water and WAD regions are then interpolated onto the model's curvilinear grid cells (Fig. 3b). There are 401×151 grid points and grid sizes vary from ~1 km near the southern open boundaries of the model domain to less than 0.5 km in the north near Anchorage, and in the Knik and Turnagain Arms. Sixteen sigma levels are used in the vertical.

Comprehensive climatology that covers the entire Cook Inlet is not available, yet temperature and salinity (*T*, *S*) are required for initial and boundary conditions. Therefore, the initial *S* is set to 32.4 psu, which corresponds approximately to the shelf/slope estimates off the Stevenson/Kennedy entrances (e.g., Xiong and Royer 1984; Okkonen and Howell 2003). With river discharges and mixing by

Table 1 Model experiments

Experiment	Stratification	Wind	River	C_z	Integration period	WAD
2Dpom	No	No	No	0.0025	30 days	No
2Dwad	No	No	No	0.0025	30 days	Yes
3Dtidehom	No	Yes	No	Variable[a]	120 days	Yes
3Dtide	Climatology	Yes	No	Variable[a]	120 days	Yes
3Driv	Climatology	Yes	Yes, high	Variable[a]	1 year[b], year 2000	Yes
3Drivsea	Climatology	Yes	Seasonal	Variable[a]	1 year[b], year 2000	Yes

[a]See Mellor (2004) and Oey (2006)
[b]One year without wind, then continued with year 2000 wind

tides, we expect that, after some time (~months), the model Inlet will establish its own salinity distribution. For temperature, data from the generalized digital environmental model (GDEM climatology; Teague et al. 1990) provides the first guess, which we modify according to NOAA/NOS' measurements at Anchorage, Seldovia, and Kodiak Island.

Cook Inlet's sea level contains large tidal components particularly M_2, S_2, K_1, and O_1 (Fig. 2). The largest of these, M_2, has an amplitude of about 1 m near the Stevenson and Kennedy entrances. To simplify the analysis without sacrificing essential WAD physics, most of the results shown below are from experiments that use a round-number period of 12 h and an average amplitude η_o=1.2 m at the model's southern open boundaries. However, we also have repeated some experiments including all tidal components. Open boundary specifications consist of a combination of normal velocity specified as a sinusoid (amplitude $\overline{U}_{no} \approx \eta_o \sqrt{g/H_{msl}}$, where H_{msl} is the average depth at ≈70 m in the lower inlet) and radiation (Oey and Chen 1992). The same specification is applied to the Shelikof Strait open boundary except that when there are river discharges Q_{river}, the same outflow is allowed to exit the model domain at the strait. The zero-phase assumption between the Shelikof Strait and Stevenson/Kennedy entrances is an excellent one. Other open-boundary specifications are as follows: one-sided advection for tangential velocities, temperature and salinity (velocities=0 and climatological T and S during inflow), Orlanski's (1976) radiation for both components for the three-dimensional velocity, and radiation based on external gravity phase speed $\sqrt{gH_{\mathrm{msl}}}$ on the relatively unimportant η (because normal velocity is specified).

We assume the Inlet is ice-free throughout the year, and at the surface, wind stresses are specified and heat and salt fluxes are zero. In the midst of winter (February), the "ice-free" assumption is a poor one near shore and in the upper Inlet (Moore et al. 2000), and the model results in these regions in winter are less reliable. That surface heat and salt fluxes are zero is also inaccurate especially in late fall and winter when strong evaporative losses are expected due to strong winds and low air temperatures. To partially compensate for the missing forcing, model surface temperature is relaxed to climatology with a timescale of 1.5 months. The surface salt flux is still zero, however, and the distribution of salinity inside the model Inlet is assumed to be dominated by discharge and mixing with more saline waters from the Gulf of Alaska. We use the NOAA/National Data Buoy Center (NDBC) buoy data and NOS winds at four stations: Anchorage, Nikiski, Drift River, and Augustine Island; examples are shown in Fig. 4 as wind stick plots for the first 60 days of year 2000. These winds are converted to stresses using Large and Pond (1981) and linearly interpolated onto the model grid. The wind is generally weaker in the upper Inlet (Anchorage) than in the lower Inlet (Augustine Island); the channeled wind along the Inlet dominates with additional short-period fluctuations, as can be seen in Fig. 4. There exist, however, finer spatial variability and transient wind events due to air flows over mountain ranges and through valleys (Orographic effects; D. Prentki, 2004, private communication); these wind events are not captured well by the use of only four stations.

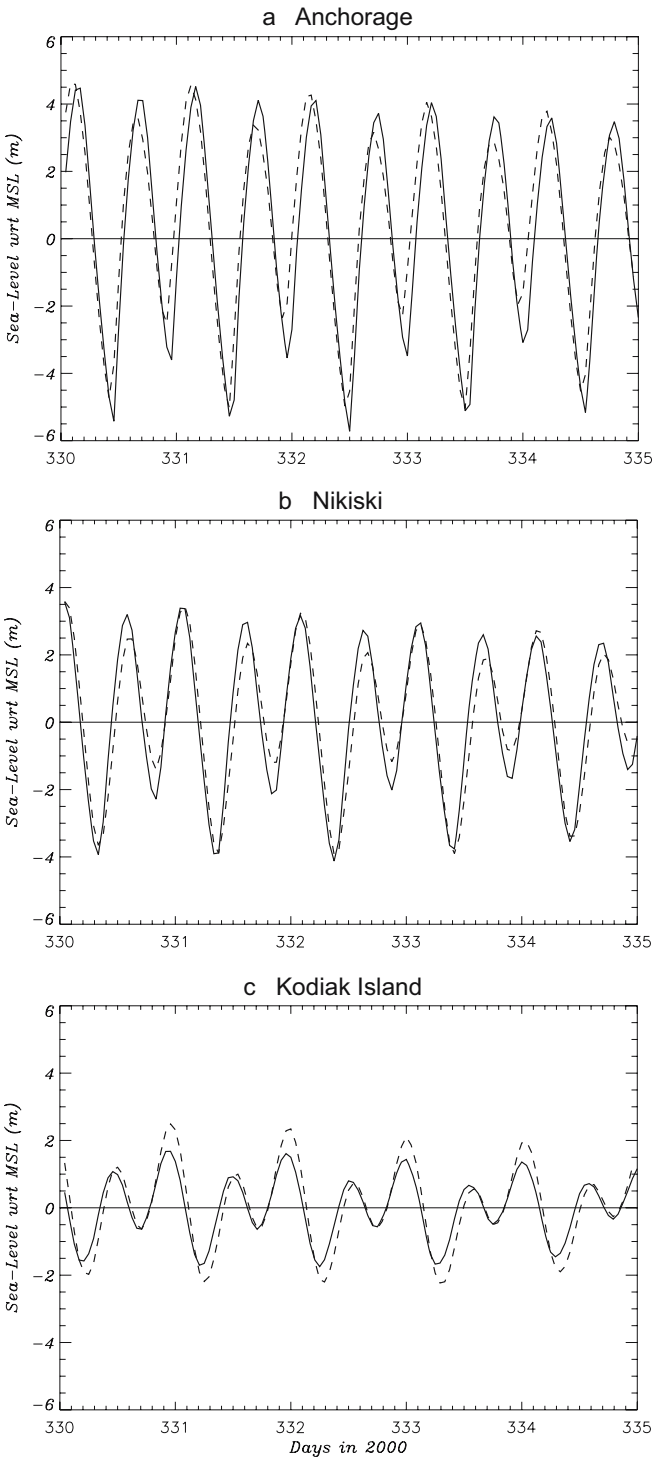

Fig. 5 Example of 5 days (in 2000) sea level variations at (from north to south) **a** Anchorage, **b** Nikiski, and **c** Kodiak Island. *Solid lines* are observations and *dash lines* are from model simulations using observed tidal forcing at the open boundaries

Discharges from seven of the larger rivers were obtained from USGS (Fig. 2). As pointed out above, the values are low estimates because USGS does not include additional contributions from tributaries. Corrections provided by Dr. Prentki were used in the model. The corrected discharge totals to about 5×10^3 m^3 s^{-1} during the summer maximum. Peak discharges occur in late spring through summer, and minima are from late fall through winter. Okkonen and Howell (2003) show that salinities measured in the lower through the middle Inlet reach lowest values in fall (October~November). The lag (between peak discharge and times of freshest Inlet's waters) suggests a tide-riverine mixing time scale of about 2~3 months. Discharge is specified as a downward vertical volume flux per unit area, w_{River} (Oey 1996). For each river, we spread w_{River} over a (somewhat subjectively determined) area in the vicinity of that river. For the rivers in the upper Inlet, the 'spreading' is often over potential WAD cells (Fig. 3)—a situation that mimics the actual spreading of fresh waters over shallow streams.

The initial field is one of rest, velocity $U=0$, S is constant=32.4 psu (as mentioned previously), and T is either stratified in the vertical, area-averaged from climatology, or homogeneous depending on model experiments (below). The water level is initially at the mean sea level (MSL). Tidal velocity forcing and/or wind and/or river are then turned on. On lateral (absolute) land boundaries, normal fluxes are nil, and no-slip conditions are applied. Bottom friction is computed either by using a bottom drag coefficient C_z obtained by matching the near-bottom

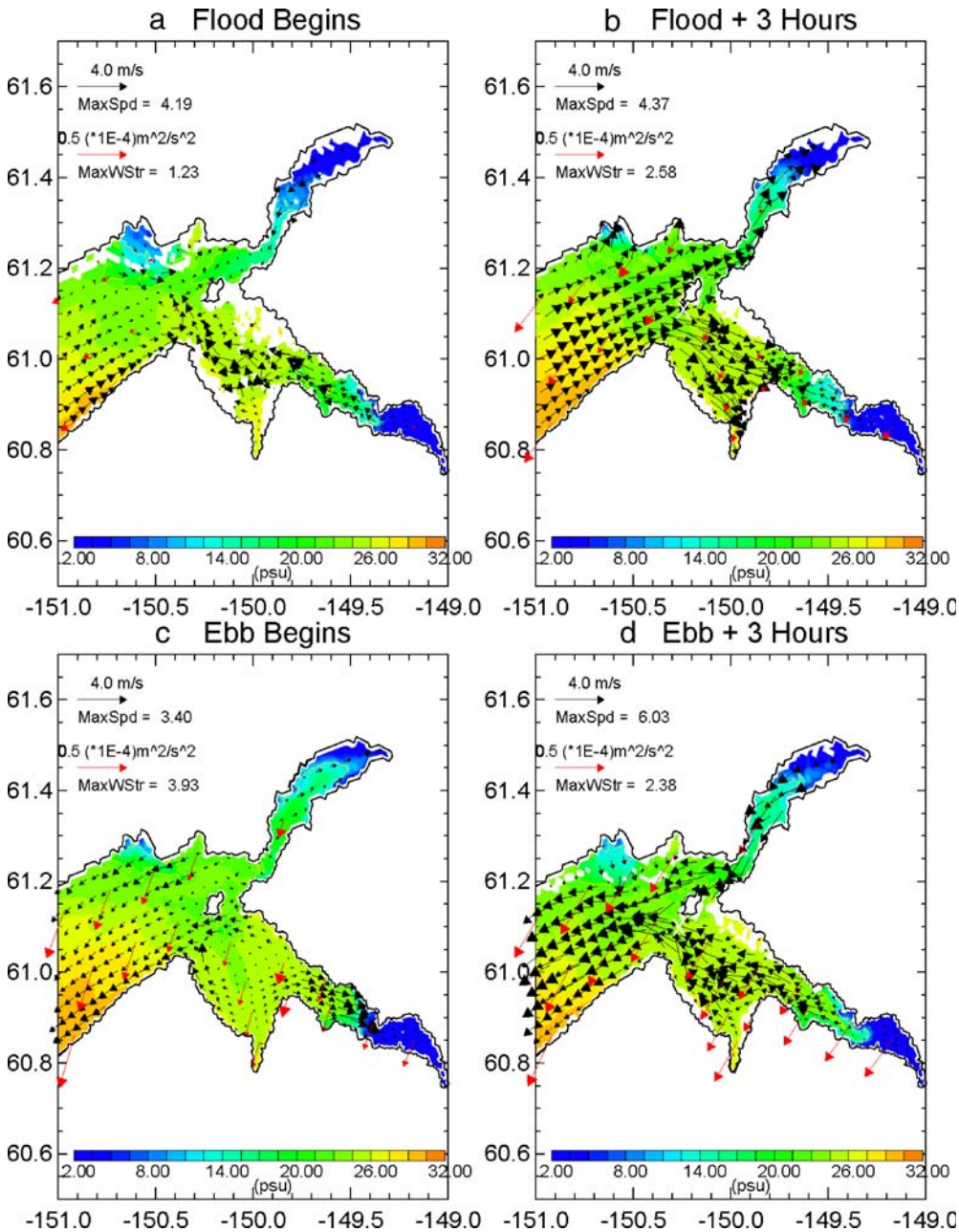

Fig. 6 Simulation of tides and river run-off in Cook Inlet, experiment 3Driv. Shown here is an enlarged region of the upper Inlet. Velocity vectors (*black*) at the first σ grid nearest the surface are shown superimposed on color images of the corresponding salinity at four different phases of a tidal cycle. *Red* vectors indicate wind stresses used in the model at the indicated dates. *Black* contour indicates the coastline and *white* regions show dry (and land) areas

modeled velocity to the Law of the Wall, or simply a constant C_z (see Mellor 2004 and the WAD implementation in Oey 2006). Smagorinsky's (1963) shear and grid-dependent formula for horizontal viscosity and diffusivity are used with their ratio=5 and the Smagorinsky's constant=0.1.

We have carried out various experiments to systematically test the model (Table 1). Experiments 2Dpom and 2Dwad are two-dimensional barotropic experiments forced only by tides at the open boundaries, but with the WAD scheme turned off (2Dpom) and on (2Dwad), respectively. For these two-dimensional calculations, quadratic bottom friction formula using the depth-averaged velocities is used, with C_z as a constant=0.0025. Experiment 3Dtidehom is the full three-dimensional POM–WAD but the water is homogeneous. The integration is for 120 days. Experiment 3Dtide is the full three-dimensional (baroclinic) POM–WAD in which stratification exists because of initial, surface, and open-boundary *T*/*S* climatology, but river discharge is nil. Experiment 3Driv turns on river runoffs. River forcing is intentionally extreme (to test POM–WAD): Corrected peak discharges (late spring through summer) from the seven rivers (Fig. 3) are specified, and they are held steady for 2 years. The total is 5×10^3 m^3 s^{-1}. Year 1 is without wind, but with tide, so that the model establishes a quasi-equilibrium state (in salinity distribution in particular). In year 2, six hourly winds that correspond to the year 2000 (linearly interpolated as described above) are also used. Finally, the experiment 3Drivsea uses seasonal river inputs instead of keeping them steady. The experiments 3Driv and 3Drivsea were conducted with both the single-component and all-component tidal forcing along the open boundaries described previously.

3 Tides and WAD processes in the upper Cook Inlet

3.1 Model simulations of tides and salinity

We focus on experiment 3Driv and discuss other cases when appropriate to draw contrasts. Because tidal resonance is an essential feature of the Cook Inlet's WAD and circulation dynamics, we first show in Fig. 5 an example of the phenomenon with plots of 5-day modeled and observed sea-levels at the lower (Kodiak), central (Nikiski), and upper inlets (Anchorage). The simulated sea level compares well with that which is observed, both in terms of the phasing and the amplification of sea level from Kodiak to Anchorage. In addition to inadequate model physics, discrepancies are in part due to inexact knowledge of the open-boundary conditions (the Kodiak Island tide station in Fig. 5c is located outside our domain, so a slight adjustment of the imposed tidal phase on the open boundary was needed). An optimal refinement of the tidal forcing as described in Chen and Mellor (1999) should improve the simulations, but this has not been done in this study.

Figure 6 shows salinity distributions at four tidal stages in the upper Inlet. At the beginning of flood (Fig. 6a), extensive "dry" areas (they are really "mudflats") can be seen south and southeast of Anchorage in the wide entrance to Turnagain Arm. "Dry" areas are also seen in the northern portion of the upper Inlet, especially in the upper Knik Arm. Three hours later (Fig. 6b), more saline flood waters begin to fill the upper Inlet. The peak flood currents are strong, up to 3~4 m s^{-1} at some location. The flooding is complete in Fig. 6c, in which one sees the filling-up of flood waters in the upper Inlet (all model grid cells are "wet" at this stage). Saline waters can clearly be seen to intrude into the two Arms. Three hours later (Fig. 6d), strong ebbing currents ensue with peak speeds of 5~6 m s^{-1}. The strong speeds (at peak flood in particular) occur in local regions where the water layer is thin (<0.5 m) and often produce supercritical flows accompanied by hydraulic jumps during the flood ("tidal bores," see below). Note that in addition to tides, Fig. 6 also shows the wind vectors (in red). However, winds are generally weak in the upper Inlet near Anchorage (Fig. 4), and we find that wind effects are usually overwhelmed by the strong tides.

3.2 Remote sensing data

The extensive "dry" regions in the Turnagain Arm south–southeast of Anchorage (seen in Fig. 6a) are well known to local residents and can be seen from the highway along the northern bank (Fig. 7). However, there are no direct measurements of the extent and variability of the mudflats. To lend support to the modeled WAD regions, we examine remote sensing data. High-resolution remote sensing data, such as those from Landsat thermatic mapper (TM) or enhanced thermatic mapper (ETM)+ (30-m resolution), are sporadic (16-day revisit time) with limited coverage (100–200 km) and high cost, not to mention the frequent cloud cover. Traditional operational satellite ocean color sensors

Fig. 7 A photo of dry regions consisting of frozen mud in the lower Turnagain Arm south-southeast of Anchorage just before the flood in the upper Cook Inlet (i.e., low tide, corresponding to approximately the tidal stage shown in Fig. 6a). The view is towards the southwest across the Inlet (this photo was taken in early March of 2005 by L.Y.O.)

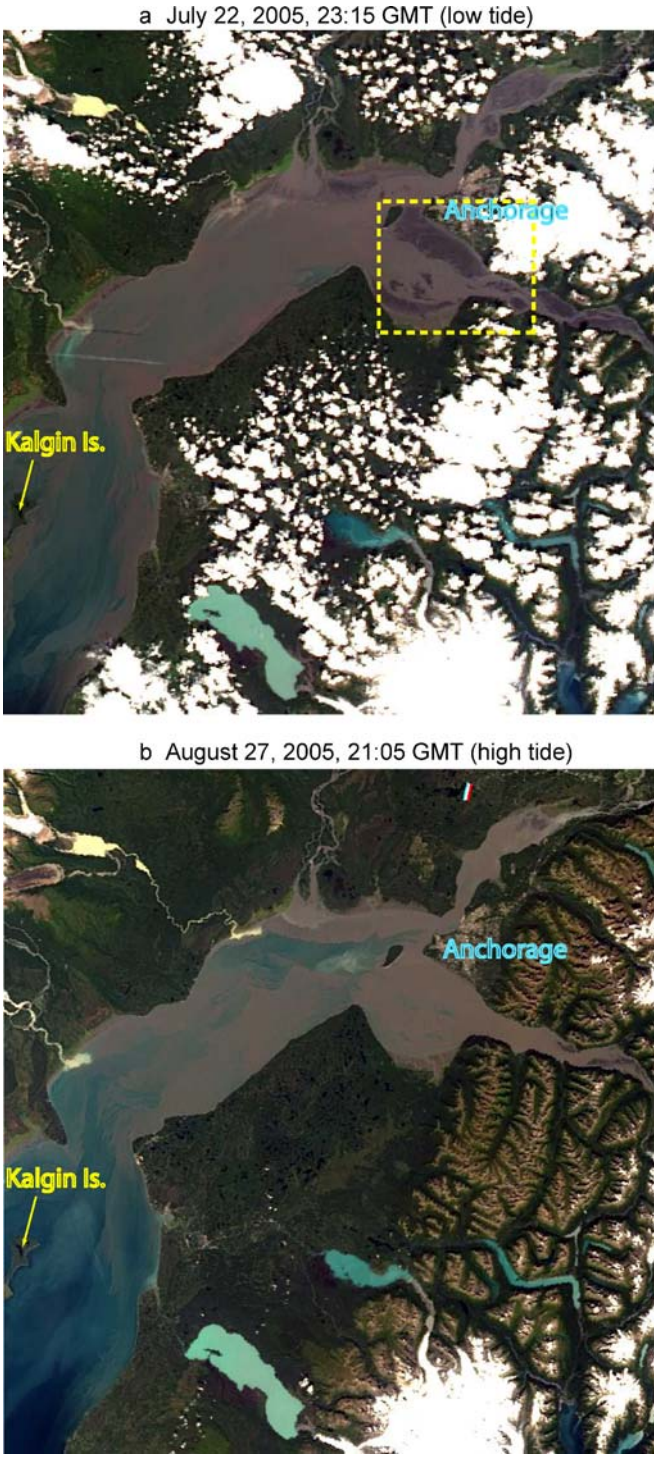

Fig. 8 MODIS/Aqua (**a**) and MODIS/Terra (**b**) true-color (RGB) images in the upper Cook Inlet: (**a**) near low tide (23:15 GMT) at Anchorage on July 22, 2005, and (**b**) near high tide (21:05 GMT) on August 27, 2005. The RGB images were composed using the three MODIS bands at 645-nm (R, 250-m), 555-nm (G, 500-m), and 443-nm (B, 500-m)

such as the coastal zone color scanner (CZCS, 1978–1986) and the sea-viewing wide field-of-view sensor (SeaWiFS, 1997–present) provide coarse resolution data at about 1-km/pixel. This is insufficient for the purpose of delineating small-scale WAD features. On the other hand, the moderate resolution imaging spectroradiometer (MODIS) instruments aboard the Terra (morning pass, 1999–present) and Aqua (afternoon pass, 2002–present) satellites are equipped with several medium-resolution bands at about 250 or 500 m/pixel. These medium-resolution data have shown unprecedented capability for coastal studies, for example, in the detection of oil spills (Hu et al. 2003) and assessment of coastal/estuarine water quality (Hu et al. 2004; Miller and McKee 2004). These data are, therefore, preferred in the present study not only because of their resolution, but also because of the repeated coverage that is available at high latitudes due to the polar orbit of the Terra

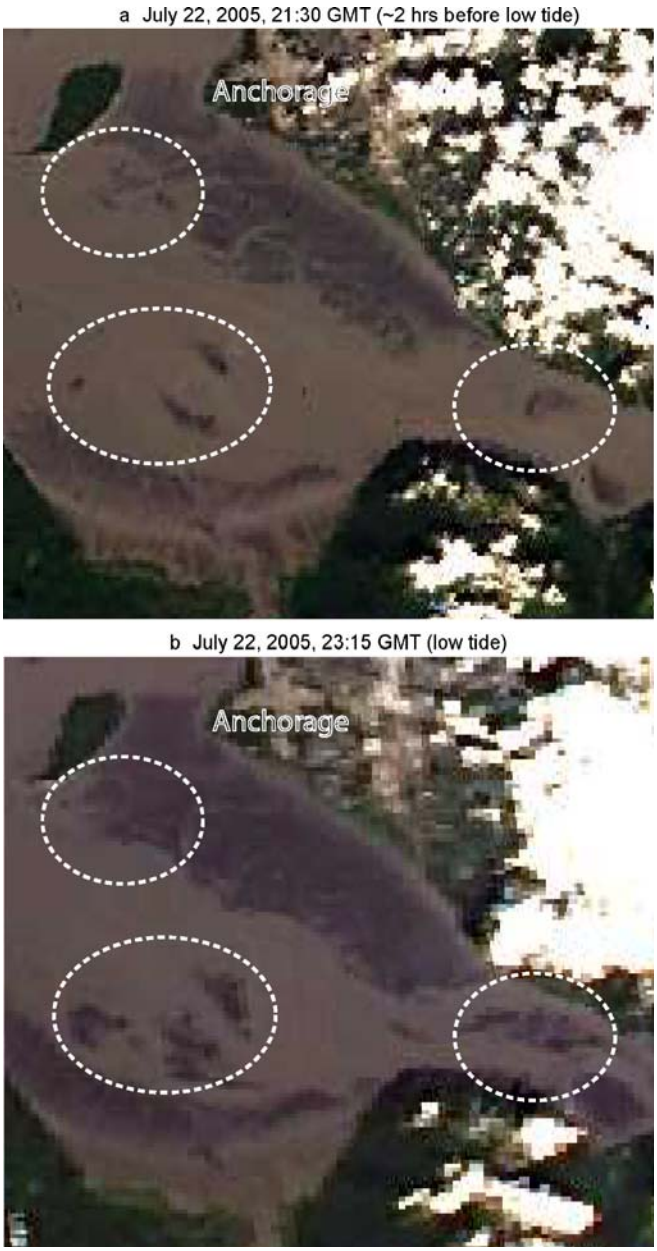

Fig. 9 Enlarged MODIS images in the region shown in Fig. 8a, for different times as indicated: (**a**) approximately 2 h before low tide at Anchorage and (**b**) near low tide. These compare the changes (areas indicated by *dashed ellipses*) in mudflat exposure during the last 2 h of low tide

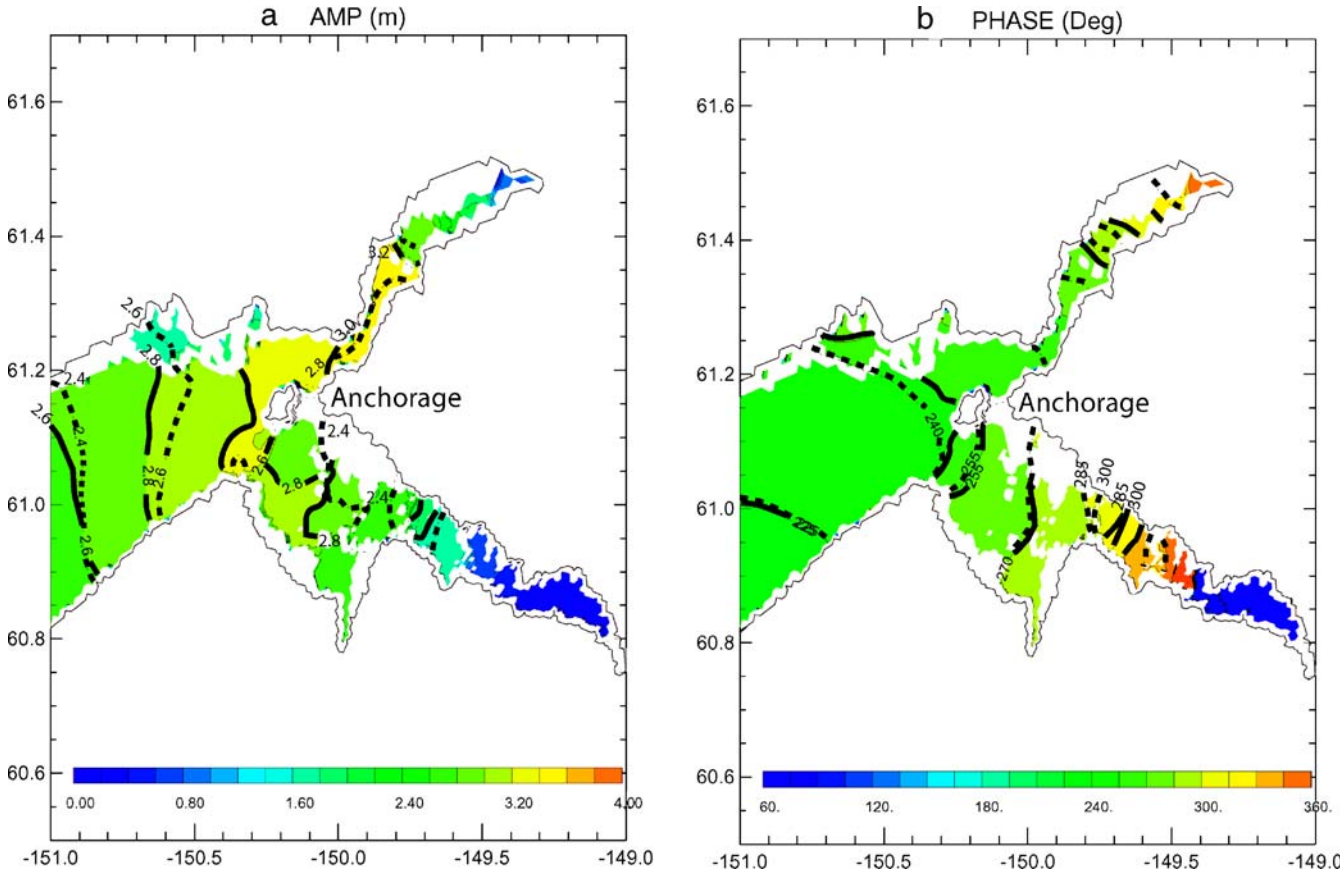

Fig. 10 Tidal (M2) amplitudes and phases for the experiment without WAD, 2Dpom (*dashed contours*) and with WAD, 2Dwad (*solid contours*; also color image) for the upper Cook Inlet

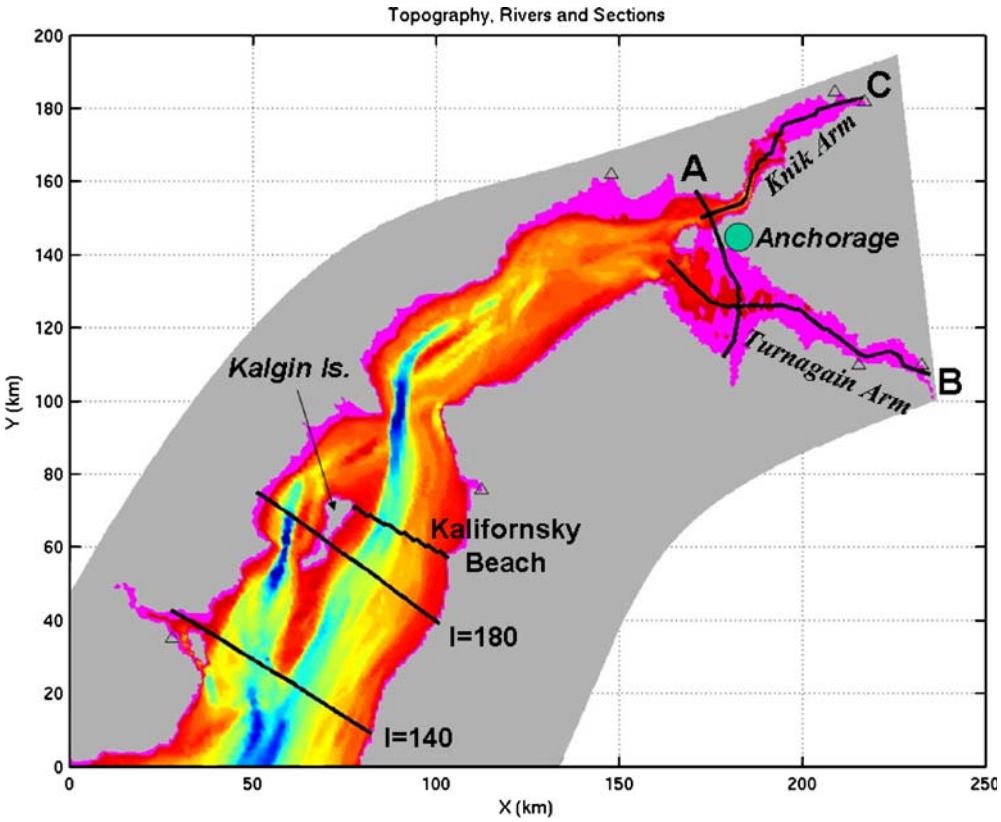

Fig. 11 Central and upper Cook Inlet topography (*colored*, scale is the same as in Fig. 3) and locations of the sections where various contours are plotted and discussed

and Aqua satellites, which allows multiple views of the Cook Inlet region within repeated tidal cycles. At the latitude of Cook Inlet, MODIS instruments provide 2–4 images per day between 21:00 and 23:50 Greenwich mean time (GMT) under ambient sunlight and during some phases of the tidal cycle. Water absorbs most of the light in the red and near infrared and is completely opaque in the mid-infrared. This makes it easy to delineate water from any other non-water surface. The absorption coefficient (a_w) of water in the blue-green wavelengths is less than 0.1 m^{-1}, but is significantly larger in the longer wavelengths. For example, at 645 and 859 nm (the MODIS 250-m bands), a_w=0.325 and 4.19 m^{-1}, respectively. Because remote sensing reflectance, R, is inversely

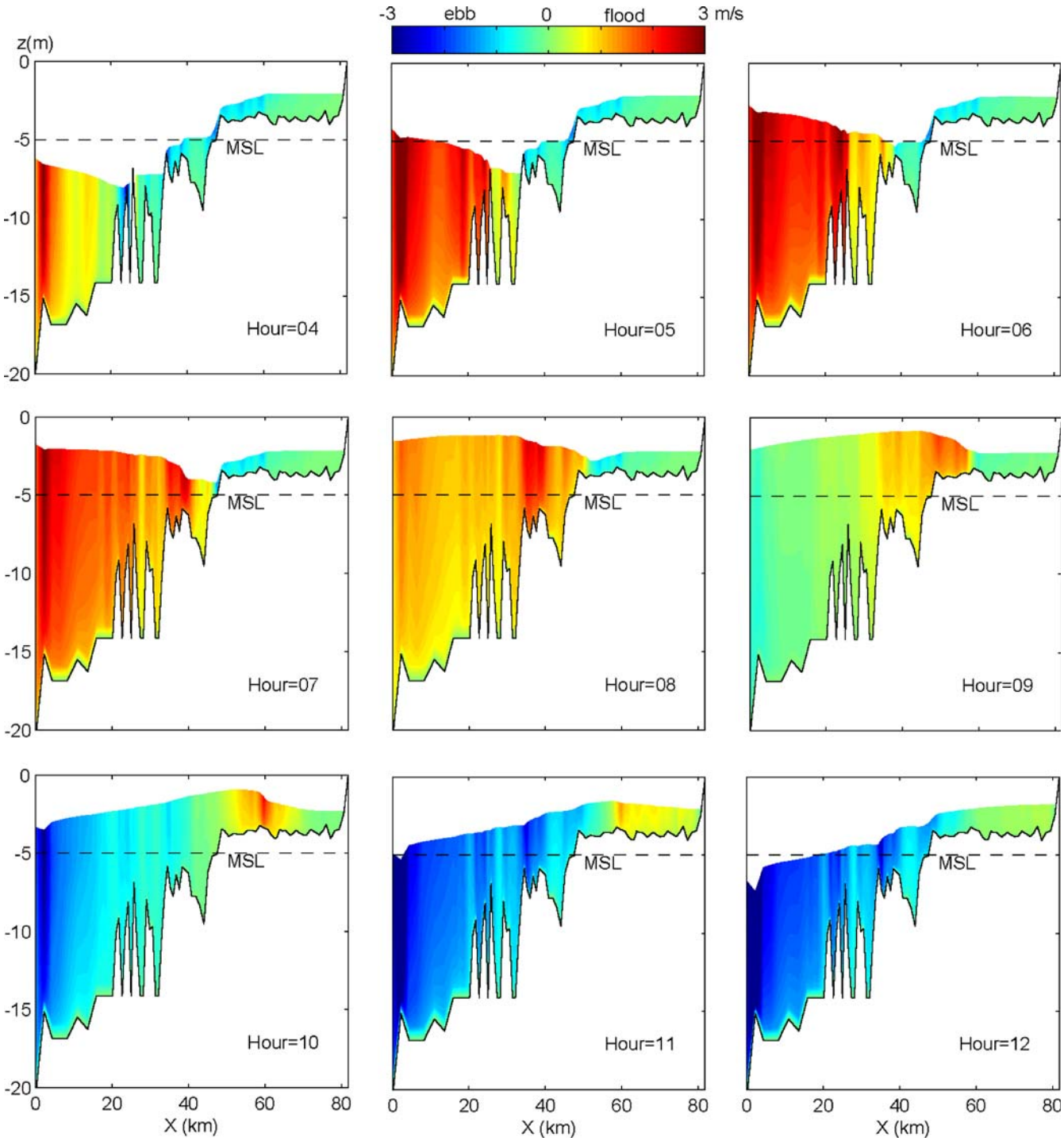

Fig. 12 Along-section velocity in Turnagain Arm (section B in Fig. 11). Shown are hourly plots starting 1 h after the beginning of flood (*Hour= 04*). *Red* indicates peak flood (i.e., southeastward flow toward the shallower region) and *blue* indicates the peak ebb. The tidal elevation (m) is also shown and the mean sea level (*MSL*) is indicated

proportional to a_w, R(859 nm) is very small (<0.001 sr^{-1}), unless there is a significant amount of suspended sediments (e.g., >100 mg l^{-1}) in the water or if the bottom is shallow (<2 m) but bright. Therefore, the 859- and 645-nm MODIS bands can be used to detect water/land interface as well as submerged land surface.

For the purpose of delineating WAD regions and (qualitatively) comparing them with the model simulation (Fig. 6), we take advantage of the periodicity of the process so that only the stage of tide is relevant rather than the actual date and time. In the following, we, therefore, choose the clearest images that are available at the appropriate tidal stages as determined from the NOS sea-level charts and compare the images with the model. Figure 8 shows the "true-color" MODIS images corresponding to approximately 1 h before a low water level at Anchorage (23:15 GMT on July 22, 2005; Fig. 8a) and 1-h before a high water level (21:05 GMT on August 27, 2005; Fig. 8b). We focus on the upper Inlet portion of the MODIS images in a domain slightly larger toward the west than that shown in Fig. 6. During low tide (Fig. 8a, which can be compared with Fig. 6a), the mudflat regions on both the northern and southern banks of Turnagain Arm (south/southeast of Anchorage) are clearly seen as darker shades of gray relative to lighter shades representing sediment-rich water. Other mudflat regions can also be seen in Fig. 8a: in the upper Knik Arm northeast of Anchorage and in the form of an arc outside a river mouth along the northern

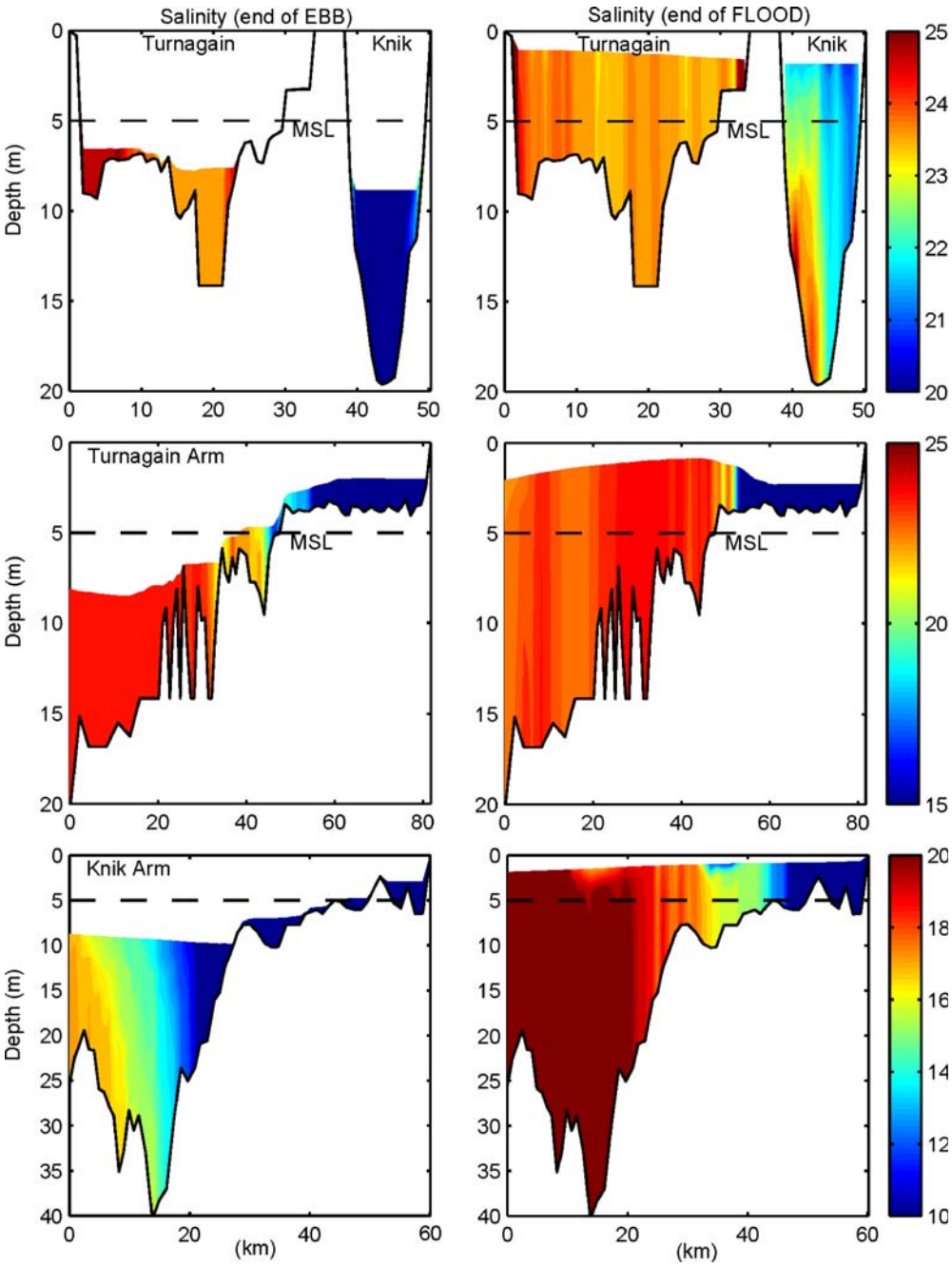

Fig. 13 Salinity in the three vertical sections shown in Fig. 11: a section (*upper panels*), b section (*middle panels*), and c section (*lower panels*). *Left panels* are at low tide and *right panels* are at high tide

coast of the upper Cook Inlet (upper center of the image). Despite the uncertainty in the detailed model topography over the mudflat areas, the satellite images are in good agreements with the predicted "dry" regions of Fig. 6a. MODIS images are useful also in delineating details of the mudflat morphology at different times. Figure 9 shows an enlarged image of the mudflat region south/southeast of Anchorage at two different times: 23:15 GMT on July 22, 2005 (lower panel; same time as in Fig. 8a) and 1 h and 45 min earlier at 21:30 GMT (upper panel). While the former shows almost-completely exposed mudflats (dark shades), the latter shows intertwined light and dark shades indicative of a more complex morphology due to unevenly submerged mudflats (the ellipses in Fig. 9 highlight the regions with significant changes; the larger ellipse is ~15 km across).

During high tide (Fig. 8b, which can be compared with Fig. 6c), most of the mudflats mentioned before are submerged and covered by murky turbid waters (brownish color) and more saline waters (clear and bluish colors) that have now penetrated from the lower Inlet. The saline intrusion is particularly pronounced along the deep channel south of the Forelands (east of Kalgin Island, lower-left corner of Fig. 8b) and will have important dynamical implications, to be discussed later in conjunction with the model results.

3.3 WAD effects on tidal amplitudes and phases

WAD processes alter the surface area and total volume of an estuary so that tidal amplitude and phases change when compared to the case without WAD. Figure 10 compares (harmonically analyzed) M2 tidal amplitudes and phases for the two cases (2Dpom and 2Dwad), focusing on the upper Inlet only (in the lower Inlet, south of the Forelands, there are only slight differences between the two cases). The comparisons are made only for those grid cells that are always wet. Large differences can be seen: Amplitudes for 2Dwad are approximately 20% larger, and the corresponding phases lag 2Dpom by about 10%. The slower phase for 2Dwad may be explained by the water-

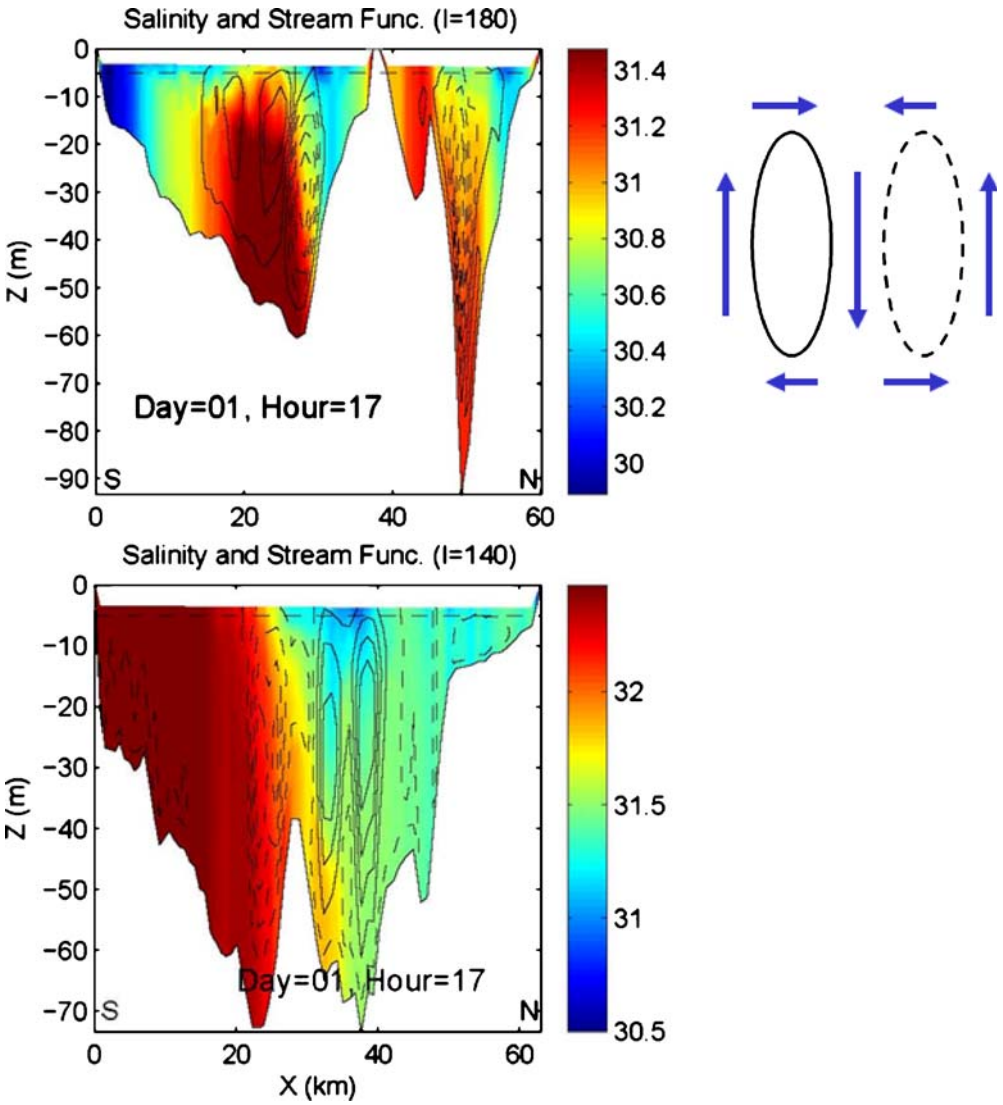

Fig. 14 Stream function (*contours*) and salinity (*colored*) at 1 h before peak (high) tide in the vertical sections "I=180" (*upper panel*) and "I=140" (*lower panel*) in the central Cook Inlet (see Fig. 11 for locations). The view is southwestward towards the lower Inlet. Solid (*dash*) stream-function contours indicate clockwise (anti-clockwise) motion in the vertical plane as indicated in the *inset*. The stream function is calculated from the cross-channel components (*V* and *W*, see the corresponding velocity values in Fig. 15)

retention property of the WAD physics that creates tidal asymmetry between flood and ebb (cf. Oey 2005). Because tidal energy fluxes into the upper Inlet through the Forelands are approximately equal for the two cases, the larger amplitudes for 2Dwad are due to its effectively smaller storage volume in the upper Inlet due to the presence of WAD areas.

3.4 Tidal bores in the Turnagain Arm

In the Science Forum website of the University of Alaska Fairbanks (http://www.gi.alaska.edu/ScienceForum/water.html), Larry Gedney observed: "Driving the Seward Highway along Turnagain Arm...one may occasionally observe a white, frothy line of turbulent water extending completely across the arm and moving slowly upstream... This is a tidal bore. It is created when rising tides in Cook Inlet encounter the constricted entrance and diminishing water depths of Turnagain Arm..." Because of large tidal ranges, currents in the upper Inlet are very strong. During a flood, the tail portion of the rising tide propagates faster than its front; the forward characteristics intersect producing a hydraulic jump that constitutes the model "bore." To examine this phenomenon, we plot vertical section contours of velocities along the Turnagain Arm (section B in Fig. 11). Figure 12 shows the along-section velocity in Turnagain Arm every hour, beginning with 1 h after the flood begins (labeled "Hour=04"). In the next 6 h (panels), one can see a bore-like structure in which the sea surface develops a 'dip' of about 2 m, propagating up the Turnagain Arm at about 3~4 m s^{-1} (10~15 km/h). These values are consistent with those given previously in Section 1. The tourist information (for those waiting to view the bore along the Arm), for example, indicates that the bore arrives at Bird Point (the middle of the shallow Arm, $X \approx 60 \sim 70$ km in Fig. 12) about 1 h after it is seen entering the shallow Arm in Beluga Point ($X \approx 50$ km). The simulations also show detailed variations in the flow velocity and wave propagation speed along the Arm. In the Turnagain Arm, for example, flood starts in the deeper part (hour=4) when the shallow region is still draining (blue colors), which produces a salinity front near $X \approx 45$ km (see Fig. 13 below).

3.5 Tidal advection and mixing of salinity in the upper Cook Inlet

Figure 13 contrasts the salinity at the three sections (A, B, and C in Fig. 11) during low (left column) and high tides. The dry areas at low tide are clearly seen for section A. Those at sections B and C cannot be seen, as rivers are specified and grid cells are always wet along the center axes of the Turnagain and Knik Arms. One sees, however, pockets of water left in local topographic 'bowls' in these Arms at low tides. In general, water along the Knik Arm is less saline, and the salinity front propagates farther into the deeper inlet than in the Turnagain Arm. There are two reasons for that asymmetry between the two Arms. First,

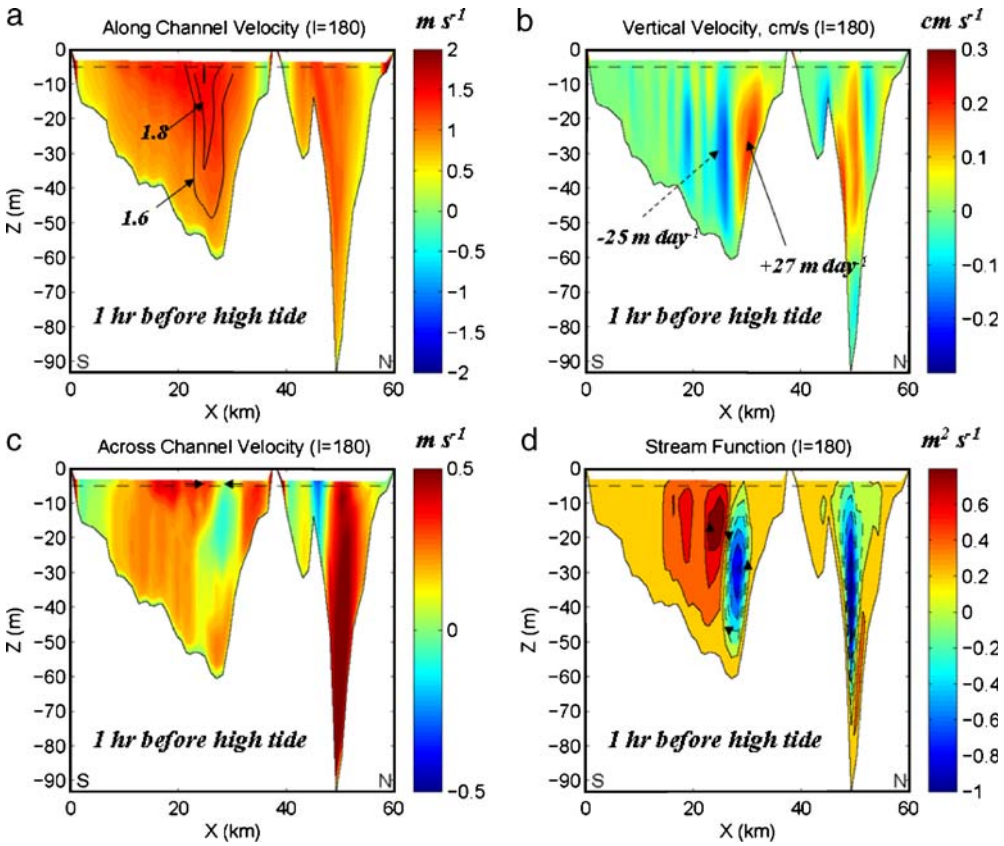

Fig. 15 Vertical sectional contours of (**a**) U, (**b**) W, (**c**) V (across-section), and (**d**) stream function at the Kalgin Island section ("I=180"; see Fig. 11 for location)

the river inputs from the Knik Arm are larger than the river inputs into the Turnagain Arm, and second, the topography along the Knik Arm is steeper compared with the flat end of the Turnagain Arm, allowing faster flushing out of waters from the Knik Arm during an ebb. Note also the strong vertical mixing produced by the tides and strong gradients across the entrance to the Knik Arm (upper right panel of Fig. 13). A similar phenomenon of strong cross-channel density gradients also occur in the central Inlet, which we now discuss.

4 Processes in the central Cook Inlet and "rip tides"

Figure 11 shows the three sections in the vicinity of Kalgin Island where strong tidal currents have been observed. Drifters launched in the central Inlet show strong tidally driven oscillatory flow, whereas the drifters are often "trapped" over the deep channel, moving back and forth for days along the channels (Dr. Mark Johnson, 2005, personal communication; http://www.ims.uaf.edu/research/johnson/cmi). The strong currents are often referred to as "rip tides" (Haley et al. 2000; Okkonen and Howell 2003), and they have scales of a few hundred meters. In the model, these features are diffused but are still discernible. We now show that these "rip tides" are due to strong fronts caused by confluences of saline (i.e., ocean) and less-saline (i.e., rivers) water masses. Stratification (horizontal and vertical) is essential for their existence. Figure 14 shows the contours of stream function superimposed on color images of salinity at the Kalgin Island section (marked "I=180" for the model grid line number) and another section some 40 km to the south ("I=140"). These contours correspond to 1 h before the peak (high) tide, and one can see the intrusion of high-salinity water due to the flooding currents on the left side of the "I=140" section, as well as in the deep channel on the left side of the Kalgin Island section (the "I=180" section). Such salinity intrusion during flood was previously noted in MODIS image in Fig. 8b. Figure 14 shows recirculating cells at both sections but particularly at the section off the Kalgin Island (I=180); the convergent region between the two opposite-signed recirculating cells defines the front at this stage of the tidal cycle. The salinity difference across the front is 1–1.5 psu. Figure 15 gives more details of the flow field at the Kalgin Island section. The figure shows strong flood (U, the through-section or along-channel component from southwest to northeast up the Inlet; Fig. 15a) with a velocity of $U \approx 2$ m s^{-1} at the frontal zone and clear convergence shown by the cross-channel velocity (V, Fig. 15c). The upwelling and downwelling velocities (Fig. 15b) of $W \approx \pm 25$ m day^{-1} create cross-channel circulation cells seen by the stream function (Fig. 15d).

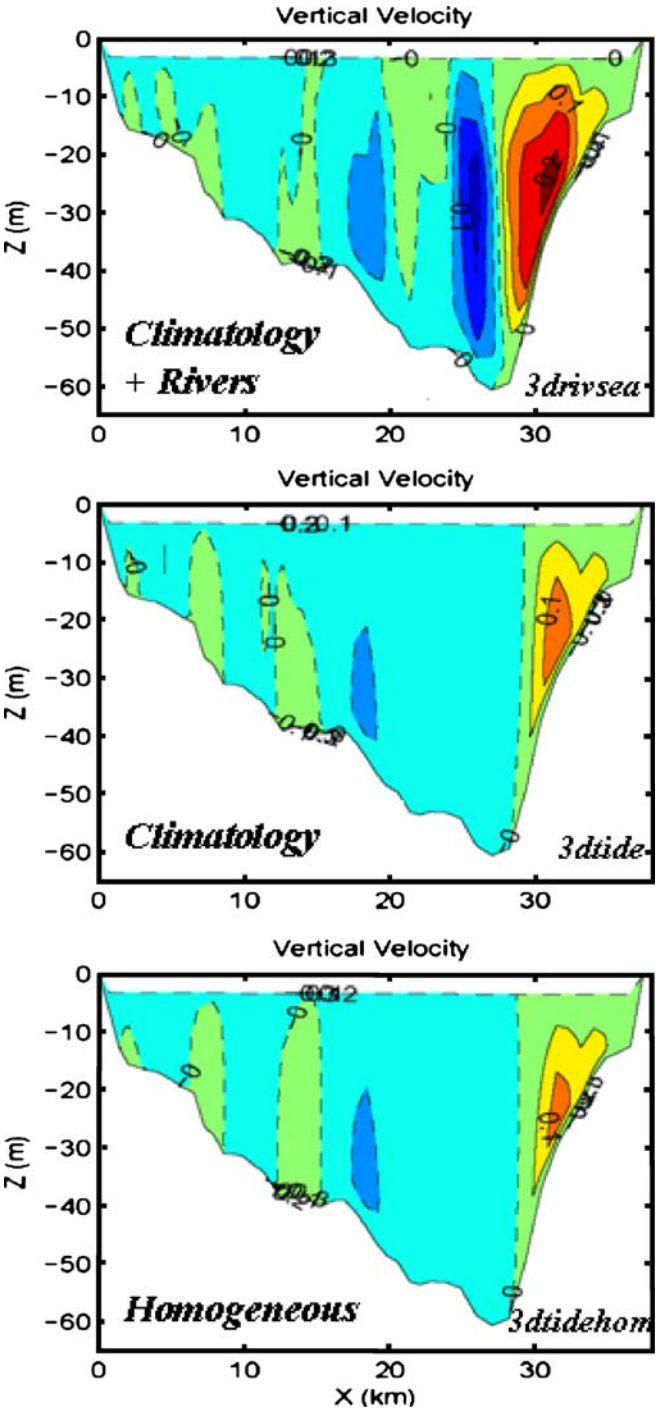

Fig. 16 Comparison of the vertical velocity contours at 1 h before high tide at the Kalgin Island section ("I=180"; see Fig. 11 for location). For clarity, only the eastern portion of that section is shown. The three cases being compared are 3Drivsea, 3Dtide, and 3Dtidehom (see Table 1 for details)

To test the importance of rivers and associated stratification in the dynamics of these circulation cells, Fig. 16 compares the results of the realistic model case with seasonal river input (3Drivsea) against the experiment (3Dtide) in which river runoffs are null (i.e., there is a weak vertical stratification from the initial GDEM climatology, but no horizontal gradients associated with fresh water input) and also against the experiment without stratification (3Dtidehom). Note that only the wider channel south of the Kalgin Island (the left part of Fig. 15b) is shown. The front over the deepest part of the channel is formed only in the case when there is river discharge (Fig. 16a) and also at

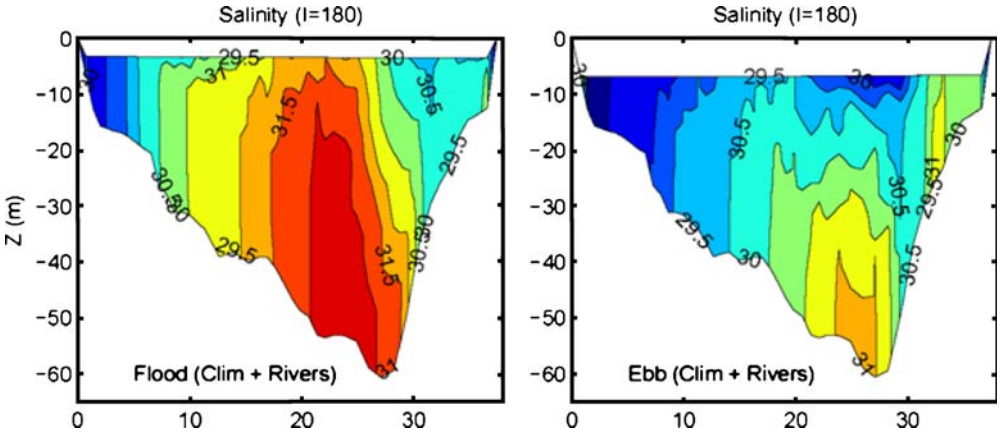

Fig. 17 Comparison of the vertical salinity contours at 1 h before peak high tide (*left panel*) and 1 h before peak ebb tide (*right panel*) at the Kalgin Island section ("I=180"; see Fig. 11 for location). For clarity, only the eastern portion of that section is shown. This case corresponds to experiment 3Drivsea (see Table 1 for details)

times of flood when large amount of saline water intrudes into the Inlet through the deep channel (Fig. 17). The model results in this study are qualitatively similar to the observations of Okkonen and Howell (2003) taken across Kalifornsky Beach (Fig. 11), although a more detailed comparison is not warranted due to the idealized nature of the model forcing we have used. Haley et al. (2000) also note that "rip tides" occur most often during flood, with strong current speeds of about 2–3 m s^{-1} east of Kalgin Island. It is quite possible that the higher observed speeds may be at times caused by the wind forcing, but the combined mechanism of tidal current and buoyancy, proposed above, is robust, i.e., the phenomenon repeats for each tidal cycle.

5 Discussion and conclusions

A WAD algorithm for POM in its most general three-dimensional settings with stratification and forcing is implemented and applied to study the WAD and circulation processes in the Cook Inlet, Alaska. The model incorporates high-resolution and realistic topography with WAD regions. The model includes tidal forcing, river discharge, temperature and salinity fields along the open boundaries, and wind forcing. Cook Inlet is an environmentally sensitive region with harsh conditions; it is an excellent place to test a model with WAD under extreme forcing that includes large tidal ranges and strong currents. Over a tidal cycle, the model simulates complex WAD regions that compare quite well with MODIS satellite images despite the uncertainty of the detailed mudflat regions. In this regard, we have demonstrated the usefulness of the fine-resolution MODIS images in detecting "dry" and "wet" regions, hence, also in evaluating the WAD processes. In the future, one may use multiple images to map the mudflat areas at different stages of the tidal cycle (with more extensive temporal and spatial coverage than that shown in this paper in Figs. 8 and 9 and with the possible usage of the near-IR and mid-IR bands) to improve the representation of the mudflat topography in the model. Identifying wet and dry pixels from the satellite images (using different channels) will provide a more quantitative data set to compare with wet and dry model cells. The same methodology may lead to improved flood predictions in other circumstances (e.g., tsunamis, storm surges, etc.). In the upper Inlet, the model simulates WAD processes that affect tidal amplitudes and phases. The model simulates the propagation of bore-like features over the shallow mudflats of the Turnagain Arm, with height and propagation speeds in rough agreements with the experiences of local observers. In the central Inlet, the model shows upwelling and downwelling cells with strong horizontal and vertical velocities. These strong currents are caused by fronts produced by the convergence of saline water from the lower inlet through the deep channel with fresher water of the upper Inlet. River inputs coupled with tides are essential to the existence of these fronts, as shown by sensitivity experiments with and without rivers. This study describes complex dynamics of an inlet with extreme tides using a model that includes the WAD algorithm. Future research may include further model evaluations and developments of new model components such as sediment transports associated with WAD and also wave-current interactions (Mellor 2003).

Acknowledgment The study was supported by the Mineral Management Service (Contract no. 1435-01-03-CT-72021); Oey and Ezer were also partly supported by Office of Naval Research (ONR) grants; Hu and Muller-Karger were supported by National Aeronautics and Space Administration (NASA) grants. The NOAA/Geophysical Fluid Dynamics Laboratory (GFDL) provided computational resources.

References

Balzano A (1998) Evaluation of methods for numerical simulation of wetting and drying in shallow water flow models. Coast Eng 34:83–107

Beaglehole JC (1974) The life of Captain James Cook. Stanford University Press, Stanford, CA, p 760

Blumberg AF, Mellor GL (1987) A description of a three-dimensional coastal ocean circulation model. In: Heaps N (ed) Three-dimensional coastal ocean models. American Geophysical Union, Washington, DC, p 208

Casulli V, Cheng R (1992) Semi-implicit finite difference methods for three-dimensional shallow water flow. Int J Numer Methods Fluids 15:629–648

Chassignet EP, Smith LT, Halliwell GR, Bleck R (2003) North Atlantic simulations with the hybrid coordinate ocean model (HYCOM): impact of the vertical coordinate choice, reference pressure and thermobaricity. J Phys Oceanogr 33:2504–2526

Chen P, Mellor GL (1999) Determination of tidal boundary forcing using tide station data. In: Mooers CNK (ed) Coastal ocean prediction, coastal and estuarine studies, vol. 56. American Geophysical Union, Washington, DC, pp 329–351

Chen C, Beardsley RC, Cowles G (2006) An unstructured grid, finite-volume coastal ocean model (FVCOM) system. Oceanography 19(1):78–89

Drillet Y, Bourdallé-Badie R, Siefridt L, Le Provost C (2005) Meddies in the Mercator North Atlantic and Mediterranean Sea eddy-resolving model. J Geophys Res 110:C03016

Ezer T, Mellor GL (2000) Sensitivity studies with the North Atlantic sigma coordinate Princeton ocean model. Dyn Atmos Ocean 32:185–208

Fan SJ, Oey L-Y, Hamilton P (2004) Assimilation of drifters and satellite data in a circulation model of the northeastern Gulf of Mexico. Cont Shelf Res 24(9):1001–1013

Flather RA, Hubbert KP (1990) Tide and surge models for shallow-water-Morecambe Bay revisited. In: Davies AM (ed) Modeling marine systems, vol. I. CRC Press, Boca Raton, FL, pp 135–166

Gill AE (1982) Atmosphere-ocean dynamics. Academic, New York, p 662

Haley B, Tomlins G, Smith O, Wilson W, Link M (2000) Mapping Cook Inlet rip tides using local knowledge and remote sensing. MMS Report, OCS Study, MMS 2000–025

Hu C, Muller-Karger FE, Taylor C, Myhre D, Murch B, Odriozola AL, Godoy G (2003) MODIS detects oil spills in Lake Maracaibo, Venezuela. Eos AGU Trans 84(33):313, 319

Hu C, Chen Z, Clayton TD, Swarzenski P, Brock JC, Muller-Karger FE (2004) Assessment of estuarine water-quality indicators using MODIS medium-resolution bands: Initial results from Tampa Bay, Florida. Remote Sens Environ 93:423–441

Ji ZG, Morton MR, Hamrick JM (2001) Wetting and drying simulation of estuarine processes. Estuar Coast Shelf Sci 53:683–700

Ko D-S, Preller RH, Martin P (2003) An experimental real-time intra Americas sea ocean nowcast/forecast system for coastal prediction. Proceedings, AMS 5th conference on coastal atmospheric and oceanic prediction and processes. AMS, New York

Large WG, Pond S (1981) Open ocean momentum flux measurements in moderate to strong winds. J Phys Oceanogr 11:324–336

Lin B, Falconer RA (1997) Three-dimensional layer-integrated modeling of estuarine flows with flooding and drying. Estuar Coast Shelf Sci 44:737–751

Lynch DR, Gray WG (1980) Finite-element simulation of flow in deforming regions. J Comp Phys 36:135–153

Marchesiello P, McWilliams JC, Shchepetkin A (2003) Equilibrium structure and dynamics of the California current system. J Phys Oceangr 33:753–783

Mellor GL (2003) The three-dimensional current and surface wave equations. J Phys Oceanogr 33:1978–1989

Mellor GL (2004) Users' guide for a three-dimensional, primitive equation, numerical ocean model. Program in atmospheric and oceanic sciences. Princeton University Press, Princeton, NJ, p 42

Mellor GL, Yamada T (1982) Development of a turbulent closure model for geophysical fluid problems. Rev Geophys Space Phys 20:851–875

Miller RL, Mckee BA (2004) Using MODIS Terra 250 m imagery to map concentrations of total suspended matter in coastal waters. Remote Sens Environ 93:259–266

Moore SE, Shelden KEW, Litzky LK, Mahoney BA, Rugh DJ (2000) Beluga, *Delphinapterus leucas*, habitat associations in Cook Inlet, Alaska. Mar Fish Rev 62(3):60–80

Oey LY (1996) Simulation of mesoscale variability in the Gulf of Mexico. J Phys Oceanogr 26:145–175

Oey L-Y (2005) A wetting and drying scheme for POM. Ocean Model 9:133–150

Oey LY (2006) An OGCM with movable land-sea boundaries. Ocean Model 13:176–195

Oey LY, Chen P (1992) A model simulation of circulation in the north-east Atlantic shelves and seas. J Geophys Res 97:20087–20115

Oey LY, Lee H-C, Schmitz WJ (2003) Effects of winds and Caribbean eddies on the frequency of loop current eddy shedding: a numerical model study. J Geophys Res 108 (C10):3324, DOI 10.1029/2002JC001698

Oey LY, Ezer T, Forristall G, Cooper C, DiMarco S, Fan S (2005) An exercise in forecasting loop current and eddy frontal positions in the Gulf of Mexico. Geophys Res Lett 32:L12611, DOI 10.1029/2005GL023253

Okkonen SR, Howell SS (2003) Measurements of temperature, salinity and circulation in Cook Inlet, Alaska. Report, OCE Study MMS 2003-036. Mineral Management Service, p 28

Orlanski I (1976) A simple boundary condition for unbounded hyperbolic flows. J Comput Phys 21:251–269

Romanou A, Chassignet EP, Sturges W (2004) The Gulf of Mexico circulation within a high resolution numerical simulation of the North Atlantic Ocean. J Geophys Res 109:CO1003, DOI 10.1029/2003CJ001770

Royer TC (1975) Seasonal variations of waters in the northern Gulf of Alaska. Deep-Sea Res 22:403–416

Sheng J, Tang L (2003) A numerical study of circulation in the western Caribbean Sea. J Phys Oceanogr 33:2049–2069

Smagorinsky J (1963) General circulation experiments with the primitive equations. Part I: the basic experiment. Mon Weather Rev 91:99–164

Smith RD, Maltrud ME, Bryan FO, Hecht MW (2000) Numerical simulation of the North Atlantic Ocean at 1/10 deg. J Phys Oceanogr 30:1532–1561

Stelling GS, Wiersma AK, Willemse JBTM (1986) Practical aspects of accurate tidal computations. J Hydraul Eng (ASCE) 9:802–817

Teague WJ, Carron NJ, Hogan PJ (1990) A comparison between the generalized digital environmental model and levitus climatologies. J Geophys Res 95:7167–7183

Wang J (1996) Global linear stability of the 2-D shallow water equations: an application of the distributive theorem of roots for polynomials on the unit circle. Mon Weather Rev 124(6):1301–1310

Wang J, Jin M, Musgrave DL, Ikeda M (2004) A hydrological digital elevation model for freshwater discharge into the Gulf of Alaska. J Geophys Res 109:C07009, DOI 10.1029/2002JC001430

Xie L, Pietrafesa LJ, Peng M (2004) Incorporation of a mass-conserving inundation scheme into a three-dimensional storm surge model. J Coast Res 20:1209–1223

Xiong Q, Royer TC (1984) Coastal temperature and salinity in the northern Gulf of Alaska. J Geophys Res 89:8061–8066